

G3Reg: Pyramid Graph-based Global Registration using Gaussian Ellipsoid Model

Zhijian Qiao, Zehuan Yu, Binqian Jiang, Huan Yin, and Shaojie Shen

Abstract—This study introduces a novel framework, G3Reg, for fast and robust global registration of LiDAR point clouds. In contrast to conventional complex keypoints and descriptors, we extract fundamental geometric primitives including planes, clusters, and lines (PCL) from the raw point cloud to obtain low-level semantic segments. Each segment is formulated as a unified Gaussian Ellipsoid Model (GEM) by employing a probability ellipsoid to ensure the ground truth centers are encompassed with a certain degree of probability. Utilizing these GEMs, we then present a distrust-and-verify scheme based on a Pyramid Compatibility Graph for Global Registration (PAGOR). Specifically, we establish an upper bound, which can be traversed based on the confidence level for compatibility testing to construct the pyramid graph. Gradually, we solve multiple maximum cliques (MAC) for each level of the graph, generating numerous transformation candidates. In the verification phase, we adopt a precise and efficient metric for point cloud alignment quality, founded on geometric primitives, to identify the optimal candidate. The performance of the algorithm is extensively validated on three publicly available datasets and a self-collected multi-session dataset, without changing any parameter settings in the experimental evaluation. The results exhibit superior robustness and real-time performance of the G3Reg framework compared to state-of-the-art methods. Furthermore, we demonstrate the potential for integrating individual GEM and PAGOR components into other algorithmic frameworks to enhance their efficacy. To advance further research and promote community understanding, we have publicly shared the source code.

Index Terms—Global registration, point cloud, LiDAR, graph theory, robust estimation

I. INTRODUCTION

ALIGNING two individual point clouds is a fundamental and indispensable operation in robotics and autonomous systems. Global registration, which estimates the transformation without prior information, has become crucial for tasks such as loop closure and relocalization [2]. The standard pipeline of global registration can typically be divided into front-end and back-end stages, which are responsible for establishing putative correspondences \mathcal{I} and estimating the transformation (\mathbf{R}, \mathbf{t}) , respectively. The transformation estimation can be formulated as a least squares problem:

$$\min_{\mathbf{R} \in \text{SO}(3), \mathbf{t} \in \mathbb{R}^3} \sum_{(x_k, y_k) \in \mathcal{I}} \rho(r(y_k, f(x_k | \mathbf{R}, \mathbf{t}))) \quad (1)$$

This work was supported in part by the HKUST Postgraduate Studentship, in part by the HKUST-DJI Joint Innovation Laboratory, and in part by the Hong Kong Center for Construction Robotics (InnoHK center supported by Hong Kong ITC).

The authors are with the Department of Electronic and Computer Engineering, The Hong Kong University of Science and Technology, Hong Kong, China. E-mail: zqiaoac@connect.ust.hk, zyuay@connect.ust.hk, bjiangah@connect.ust.hk, eehyin@ust.hk, eeshaojie@ust.hk.

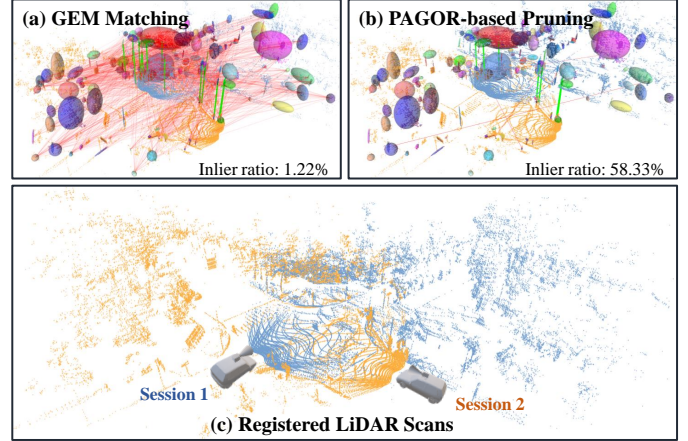


Figure 1. Global registration procedure using our proposed G3Reg. (a) Front-end GEM matching for Gaussian ellipsoid modeling and correspondence building. (b) Back-end PAGOR for outlier pruning and pose estimation under a distrust-and-verify scheme. (c) A challenging global registration result at a road intersection, in which the two LiDAR point clouds are with low overlap and a large view difference.

where $\rho(\cdot)$ represents the robust kernel function, $r(\cdot)$ is the residual function, and $f(\cdot)$ denotes the rigid transformation.

Conventional approaches rely on complex keypoint and descriptor extraction using handcrafted methods [3] or deep learning-based local descriptors [4] to establish \mathcal{I} . However, they face challenges such as excessive processing time and reduced descriptor discriminability due to uneven density and varying viewpoints. The latter challenge can lead to an extremely high outlier ratio (e.g., 99%), significantly undermining the quality of registration.

To address this issue, recent advances [1, 5]–[9] suggest utilizing maximal clique inlier selection and coupling it with a robust estimator for transformation estimation. The inlier clique has been proven to belong to at least one maximal clique in the compatibility graph [5]. To efficiently find this maximal clique, the maximum clique with the largest cardinality is computed. However, this strategy does not always work due to inappropriate threshold selection in the compatibility test [7], especially under extreme viewpoint changes and repetitive patterns, as discussed in [10].

In this study, we present a novel framework, named G3Reg, for the global registration of LiDAR point clouds that effectively addresses these issues. Our first key insight is to use segments and classify them into geometric primitives (planes, clusters, and lines) as a replacement for complex keypoints and descriptors. This approach has two advantages: firstly, using segments directly avoids the loss of geometric information

caused by traditional keypoints; secondly, it eliminates the need for complex keypoint and descriptor extraction, thus reducing computational time. Our second key insight is a novel distrust-and-verify scheme that generates multiple transformation candidates and leverages compressed raw point clouds to verify and select the most appropriate candidate. Specifically, multiple maximum cliques are obtained by constructing a pyramid compatibility graph using a traversable confidence-related upper bound for the compatibility test. Each maximum clique is then used to estimate a transformation candidate.

This work is an extended version of our earlier conference paper [10]. In comparison, the journal version presents several notable enhancements, including a more efficient front-end approach that eliminates the need for the semantic segmentation network. Additionally, we have significantly improved our distrust-and-verify framework in terms of both efficiency and robustness. The contributions of this work are outlined as follows:

- We introduce a novel segment-based front-end approach to obtain putative correspondences. In this approach, each segment is parameterized by the proposed GEM, which lays the groundwork for the following multi-threshold compatibility test and enables distribution-to-distribution registration at the back end.
- We propose a distrust-and-verify scheme that generates multiple transformation candidates by distrusting the compatibility test and verifying their point cloud alignment quality. To achieve this, a pyramid compatibility graph is constructed using the multi-threshold compatibility test, and a graduated MAC solver is proposed to solve the maximum clique on each level. Finally, transformation candidates are estimated from these cliques, and an evaluation function is designed to select the optimal one.
- We conduct extensive evaluations of our proposed G3Reg on three publicly available datasets and a self-collected multi-session dataset in the real world. The experimental results demonstrate the superiority of our proposed method in terms of robustness and real-time performance compared to state-of-the-art handcrafted and deep learning methods.
- To enhance comprehension and encourage the adoption of our framework, we have released our source code ¹ as open-source to the community. Our framework not only facilitates the replication of experiments but also offers the flexibility to modify individual components like detectors, matchers, maximum clique solvers, transformation estimators, and scalability to suit different datasets.

II. RELATED WORK

Global point cloud registration can be categorized into two primary models: correspondence-free and correspondence-based. The correspondence-free model achieves global registration using techniques like Fourier analysis [11], branch and bound strategies [12], and learned feature alignment techniques [13, 14]. However, correspondence-free models are

generally time-consuming for global transformation search. This paper proposes a correspondence-based method, which involves various modules, including discriminative keypoint detection, descriptor extraction, efficient correspondence ranking for outlier pruning, and robust transformation estimation. In this section, we delve into related works that concentrate on these individual modules.

A. 3D Point Matching

1) *3D Keypoint Detection*: The process of 3D point matching involves two main steps: keypoint detection and descriptor designing. In the case of LiDAR point clouds in large-scale scenes, keypoint detection is crucial for reducing the number of point clouds that require registration, thus alleviating the burden on the registration algorithm.

Manual keypoint detection methods use local geometric properties to assess the saliency of a point. For example, ISS [15] uses the eigenvalue ratio of the neighborhood covariance matrix to evaluate point prominence. Similarly, KPQ [16] utilizes the largest eigenvalue ratio to identify candidate keypoints and calculates curvature for prominence estimation. In the case of vehicle-mounted LiDARs, Link3D [17] introduces a scheme that clusters edge points in the vertical direction to extract Linear Keypoints Representations. On the other hand, the deep learning method D3Feat [18] predicts keypoint scores for each point in dense point clouds, assigning higher scores to matchable matches.

In practical applications, LiDAR-based keypoint detection methods are often affected by factors like noise, occlusion, and point cloud density, resulting in poor repeatability. Additionally, keypoints may discard important geometric information, such as cluttered vegetation and smooth walls. Therefore, methods like Segmatch [19] and BoxGraph [20] have been developed, which extract segments to represent point clouds and use their centers for registration. Segment-based registration methods retain the structural information of the entire point cloud, showing robustness to noise and density variations. However, the repeatability of their center estimation is significantly influenced by viewpoints.

In our proposed method, we also utilize segments for global registration. The key difference lies in our introduction of a plane-assisted segmentation method to achieve segments with higher repeatability. Additionally, we employ GEM to model the uncertainty of segment centers, ensuring probabilistic coverage of the ground truth center. This approach enhances the robustness and accuracy of our registration process.

2) *3D Descriptor-based Matching*: An ideal local descriptor should possess several key characteristics, including invariance to geometric transformations, discriminative properties, and high generalizability across different scenarios. To achieve rotation invariance, the Fast Point Feature Histogram (FPFH) [3] computes rotation-invariant features such as distances and angles between points and normals. Building upon this, PPFNet [21] and RPMNet [22] utilize neural networks to extract features from these fundamental attributes. Another approach involves calculating a local reference frame (LRF), demonstrated by SHOT [23] and SpinNet [24]. However,

¹<https://github.com/HKUST-Aerial-Robotics/G3Reg>

inaccuracies in LRF estimation due to noise and density variations can pose challenges. To address this, GeDi [25] employs a quaternion transformation network (QNet) to canonicalize patches with respect to their local reference frame, ensuring robustness to such variations. Furthermore, RoReg [26] introduces the icosahedral group and rotation-equivariant layers to achieve rotation equivariance, leading to rotation invariance through average pooling.

In addition to sophisticated descriptor design, training strategies also play a crucial role in deep learning-based methods. For example, data augmentation based on random rigid-body transformations can be employed to increase invariance to geometric transformations. Additionally, the use of hard-contrastive and hard-triplet losses [4] can enhance the discriminability and generalization ability of learned descriptors. These strategies contribute to the effectiveness and robustness of deep learning-based descriptor methods.

After obtaining 3D descriptors, the mutual-nearest neighbors (MNN) method is commonly used to establish putative correspondences. However, MNN may encounter degeneracy situations where the number of true inliers drops below three, leading to registration failure. An alternative and more conservative approach is to utilize all-to-all correspondences, considering all possible pairwise matches but potentially resulting in a high outlier ratio.

In our study, combining the strengths of both paradigms, we employ a weak descriptor and a mutual-K-nearest neighbors (MKNN) matching strategy to establish the initial correspondence set \mathcal{I} in Problem (1). Although the outlier ratio may remain high with this approach, it effectively prevents degeneracy in most situations, ensuring a more robust registration.

B. Outlier Pruning

The robust loss function $\rho(\cdot)$ in Problem (1) is known for effectively rejecting outliers, but it may face challenges when dealing with problems involving high outlier ratios, such as up to 99% outliers. To reduce the outlier ratio to a level where existing solvers (such as RANSAC and GNC [27]) perform well, a common approach in the computer vision community involves employing reciprocity checks and ratio tests [28]. Unlike the aforementioned approaches that heavily rely on descriptor performance, GORE [29] reformulates the problem, leveraging deterministic geometric properties to establish an upper bound on the inlier set size subproblem and a lower bound on the optimal solution, effectively eliminating incorrect matches.

In recent years, graph-theoretic methods have emerged as powerful tools in various registration works, demonstrating exceptional performance regardless of descriptor quality. Based on the compatibility graph, Enqvist *et al.* [30] propose using vertex cover to identify mutually consistent correspondences. MV (Mutual Voting) [31] introduces a mutual voting method for ranking 3D correspondences, enabling vertices and edges to refine each other in a mutually beneficial manner. Another widely used and stricter algorithm is the maximal clique inlier selection [1, 5, 6, 9, 32, 33], which requires every correspondence to be mutually compatible. However, finding

the maximal clique is known to be an NP-hard problem, and its runtime often becomes impractical as the number of correspondences increases. To address this challenge, ROBIN [7] proposes a faster alternative by computing the maximum k -core of the graph.

In our proposed method, we also adopt the maximum clique approach but introduce a traversable confidence-related threshold to construct a pyramid compatibility graph and solve multiple maximum cliques in a graduated manner. This approach effectively increases the probability that inliers make up one of the solved maximum cliques.

C. Robust Transformation Estimation

Robust transformation estimation has been extensively studied in various research fields [34]. It can be formulated using different approaches, including least trimmed squares (LTS) in classical robust statistics [35], consensus maximization (MC) in computer vision [36], quadratic pose estimation problems [37], and truncated least squares (TLS) in robotics [5, 38]. Trimmed ICP [35] selects potential inlier correspondences and estimates the transformation using a predefined trimming percentage, which is often unknown in real applications. On the other hand, MC defines a consensus set that contains consistent correspondences with residuals below a threshold and aims to find the optimal (\mathbf{R}, \mathbf{t}) that maximizes the size of the consensus set. However, MC becomes NP-hard [39] when $\mathbf{R} \in \text{SO}(3)$, leading to the adoption of the suboptimal but efficient RANSAC algorithm to find the outlier-free set. Nevertheless, the runtime of RANSAC increases exponentially with the outlier rate.

In this study, we formulate the registration problem as a truncated least squares (TLS) problem. To address this problem, we leverage the Black-Rangarajan duality [40] to rewrite TLS using the corresponding outlier process. To solve the TLS problem, we adopt the fast heuristic Graduated Non-Convexity (GNC) algorithm based on alternating optimization [27]. The GNC approach starts with a convex approximation of the cost function and gradually refines it to recover the original function. By employing graph-theoretic outlier pruning, GNC performs well in scenarios with moderate outlier rates, such as 80%. The primary difference between our formulation and conventional ones [5] lies in the usage of a distribution-to-distribution residual rather than a point-to-point residual, following a similar approach to Generalized ICP (GICP) [41].

III. PROBLEM FORMULATION

Given two 3D LiDAR point clouds, denoted as \mathcal{X} and \mathcal{Y} , our primary goal is to estimate the optimal rigid transformation, represented as $(\hat{\mathbf{R}}, \hat{\mathbf{t}})$, that best aligns the source point cloud \mathcal{X} with the target point cloud \mathcal{Y} . To achieve this, we first extract Gaussian Ellipsoid Models (GEM) from the segments within the point clouds during the front-end processing phase (Section IV). Consequently, we can denote \mathcal{X} and \mathcal{Y} as a series of GEMs, $\{x_1 \dots x_{N_x}\}$ and $\{y_1 \dots y_{N_y}\}$ respectively.

In the subsequent back-end phase of the framework, our strategy for estimating the optimal transformation parameters

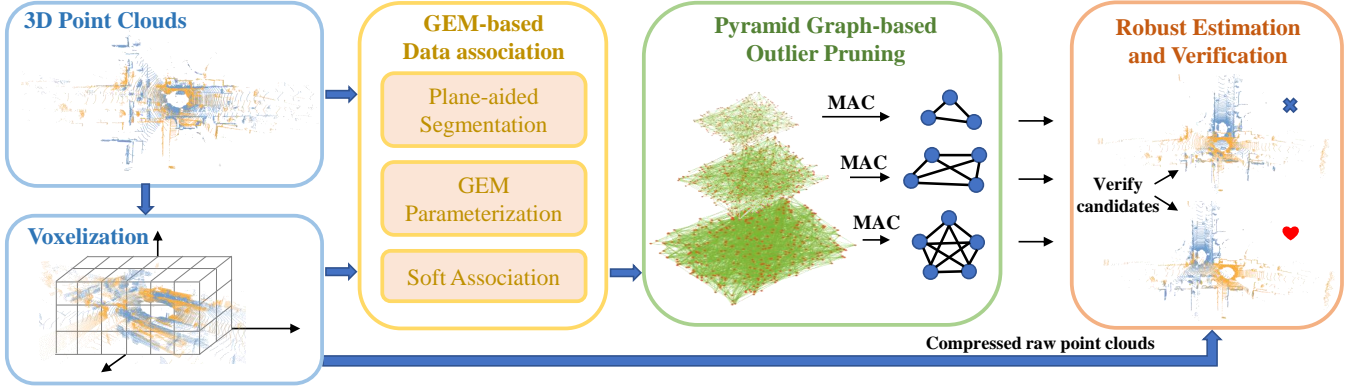


Figure 2. The proposed global registration method G3Reg adopts a distrust-and-verify framework, consisting of three components. First, putative correspondences between input point clouds are established via GEM-based data association (block in yellow). Then a pyramid compatibility graph is constructed to generate maximal cliques to obtain transformation candidates (block in green). Finally, the original point cloud information is re-utilized to select the optimal candidate (block in brownish-orange).

$(\tilde{\mathbf{R}}, \tilde{\mathbf{t}})$ employs a distrust-and-verify scheme. This scheme generates multiple transformation candidates using the extracted GEMs and then selects the most probable candidate that optimally aligns \mathcal{X} and \mathcal{Y} .

To hypothesize a candidate transformation $(\mathbf{R}^*, \mathbf{t}^*)$, we construct a compatibility graph (Section V-A) for the original putative correspondence set \mathcal{I} and derive a potential inlier set \mathcal{I}^* by identifying the maximum clique within the graph (Section V-C). We adapt the formulation presented in Equation (1) to express the registration problem as follows:

$$\mathbf{R}^*, \mathbf{t}^* = \min \sum_{(x_k, y_k) \in \mathcal{I}^*} \rho(r(y_k, f(x_k | \mathbf{R}, \mathbf{t}))) \quad (2)$$

In this equation, \mathcal{I} is replaced with \mathcal{I}^* compared to the formulation in Equation (1). The robust loss function $\rho(\cdot)$ and the residual function $r(\cdot)$ of two associated GEMs are defined in Section VI-A.

By traversing the compatibility test threshold across various confidence levels (Section V-B) to construct a pyramid compatibility graph, we can derive multiple potential \mathcal{I}_m^* from their maximum cliques. We can then solve the corresponding hypothetical transformation $(\mathbf{R}_m^*, \mathbf{t}_m^*)$ using Equation (2). Subsequently, we introduce an evaluation function g (Section VI-B) to determine the most suitable transformation based on the geometric information of \mathcal{X} and \mathcal{Y} , as follows:

$$\tilde{\mathbf{R}}, \tilde{\mathbf{t}} = \arg \min_{\tilde{\mathbf{R}} \in \{\mathbf{R}_m^*\}, \tilde{\mathbf{t}} \in \{\mathbf{t}_m^*\}} g(\mathbf{R}_m^*, \mathbf{t}_m^* | \mathcal{X}, \mathcal{Y}) \quad (3)$$

In summary, our proposed G3Reg method firstly introduces the novel concept of GEM and utilizes it to obtain the putative correspondence set. It then follows a carefully designed distrust-and-verify framework that facilitates fast and robust registration.

IV. GEM-BASED DATA ASSOCIATION

In this section, we present our method for extracting Gaussian Ellipsoid Models (GEMs) from two given point

clouds and acquiring the initial putative correspondences, \mathcal{I} . This entire procedure is composed of three steps. First, we design a plane-aided segmentation algorithm to process the input LiDAR scans, resulting in a series of plane, line and cluster (PCL) segments (Section IV-A). Second, for each of these segments, we model it as a GEM. This is achieved by estimating its statistical Gaussian distribution parameters along with an additional pseudo-Gaussian parameter (Section IV-B). Lastly, based on the GEM parameters, we select a subset of these GEMs that are deemed significant and implement a soft association strategy. This strategy is facilitated through the use of mutual K nearest neighbors (Section IV-C).

A. Plane-aided Segmentation

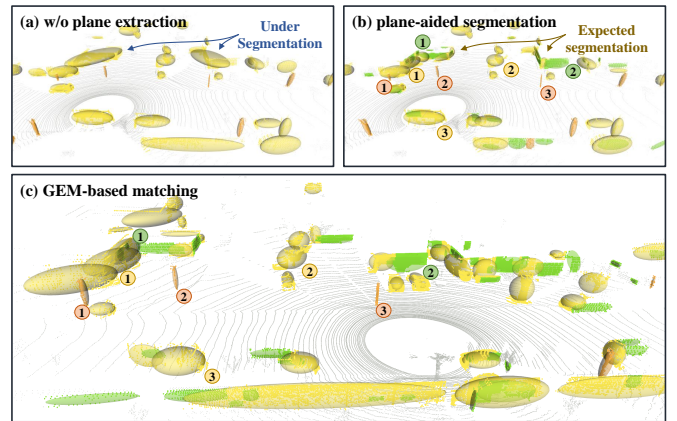


Figure 3. Visualization of GEM-based data association. Green, yellow, and orange represent planes, clusters, and lines respectively. (a) and (b) show the difference in segmentation results without or with plane assistance. As the arrow indicates, the former leads to under-segmentation. (c) is a different frame from (b). We use different colors and indices to illustrate the matching between GEMs of these two frames.

The initiation of GEM extraction involves identifying repeatable segments within a LiDAR point cloud from varying viewpoints. We segment point clouds with reference to TRAVEL [42]; however, a significant distinction lies in our

categorization of the resulting segments into three types: planes, lines, and clusters (PCL). This methodology is underpinned by three considerations. First, planes and lines, being distinct geometric structures, are advantageous for precise point cloud registration. Second, plane segmentation helps prevent extensive portions of the point cloud segments from being incorrectly merged, resulting in under-segmentation. This strengthens the repeatability of the derived clusters. Lastly, these low-level semantics assist in data association. Figure 3 presents a visual comparison of outcomes obtained with and without plane-assisted segmentation, and also the GEM-based matching proposed in our approach.

More specifically, we first voxelise the point cloud with a voxel size of s_v , and determine whether each voxel forms a plane based on the ratio of the smallest eigenvalue λ_3 to the second smallest eigenvalue λ_2 and its threshold σ_p . We then apply region growing to merge plane voxels into plane segments. The decision to merge plane voxels is predicated on several factors, including point-to-plane distance, the similarity of normal vectors n_1 and n_2 , and adjacency relations. These conditions are elaborated as follows:

- 1) Distance condition: $abs(n_1^T(p_1 - p_2))$ and $abs(n_2^T(p_1 - p_2))$ are smaller than a threshold σ_{p2n} . Here, p represents the center of plane points.
- 2) Normal condition: $abs(n_1^T n_2)$ is smaller than a threshold σ_n .
- 3) Adjacency condition: two planes should contain at least one voxel that is adjacent to each other.

Subsequently, we employ TRAVEL [42] to segment the remaining point cloud into clusters. Furthermore, for each cluster, we employ RANSAC to fit a line, employing a point-to-line distance threshold σ_{p2l} . Clusters that exhibit an inlier rate exceeding a predefined threshold σ_{line} are identified as lines. Ultimately, every voxel is re-labeled based on the segmented PCL segments and is used in the verification stage for evaluating alignment quality (Section VI-B).

B. Parameter Estimation

Data Structure 1: Gaussian Ellipsoid Model

1	Struct GEM:
2	PCL type; % Plane, cluster or line
3	Vector3 μ ; % Statistical center
4	Matrix3 Σ ; % Statistical covariance
5	Matrix3 $\hat{\Sigma}$; % Pseudo covariance
6	Vector3 $\hat{\lambda}$; % Eigenvalues of $\hat{\Sigma}$
7	end

In this section, we represent the low-level semantic segments obtained in the previous step via a standardized parameterization mentioned as the Gaussian Ellipsoid Model (GEM). The attributes of the GEM are outlined in **Data Structure 1**. Each GEM's type is associated with its specific geometric primitive. We directly derive the statistical Gaussian

distribution parameters from the parameters of the contained voxels, thereby eliminating the need for recomputation:

$$\begin{aligned}\mu &= \frac{1}{\sum_{k=1}^{N_v} N_k} \sum_{k=1}^{N_v} N_k \mu_k \\ \Sigma &= \frac{1}{\sum_{k=1}^{N_v} N_k} \sum_{k=1}^{N_v} (N_k (\Sigma_k + \mu_k \mu_k^T)) - \mu \mu^T\end{aligned}\quad (4)$$

where N_v is the number of contained voxels, and N_v and (μ_k, Σ_k) denote the point number, statistical center and covariance matrix of the k -th voxel, respectively.

Generally, the distribution of an object in the real world adheres to a uniform distribution. Therefore, the use of statistical Gaussian covariance as a descriptor may result in distortions and limitations, particularly when confronted with variations in point density. To address this issue, we introduce pseudo-Gaussian parameters to model the uncertainty associated with a segment's center point μ , based on Assumption 1, as illustrated in Figure 4.

Assumption 1 (Probability Coverage of Center). *Given an observed segment, the observation's incompleteness implies that the statistically derived μ cannot represent its true center $\hat{\mu}$. However, we expect $\hat{\mu}$ to converge within the minimal 3D Oriented Bounding Box (OBB) that encloses the segment, with a high degree of probability. Moreover, the difference $\delta\mu$ between μ and $\hat{\mu}$ is constrained within this 3D OBB, as both μ and $\hat{\mu}$ converge within it.*

Following this assumption, we estimate pseudo-Gaussian parameters in two stages. Initially, we regress the 3D OBB by projecting the points onto a 2D plane along a specified axis (normal for plane and cluster, direction for line). We then derive the 2D OBB from the projected points as per [43]. The 3D OBB is finally attained by merging the 2D OBB with its projection axis.

In the subsequent stage, we derive the 3D Oriented Bounding Ellipsoid (OBE) that is tangential to the 3D OBB and designate it as the probability ellipsoid for the center point μ of the GEM. Assuming that $\mu \in \mathcal{N}(\hat{\mu}, \hat{\Sigma})$, this probability ellipsoid can be represented as follows:

$$(\mu - \hat{\mu})^T \hat{\Sigma}^{-1} (\mu - \hat{\mu}) \leq \chi_{(p)}^2 \quad (5)$$

where $\chi_{(p)}^2$ is the 3-DoF χ^2 value with a probability $(1 - p)$ to reject the possible center outside of the ellipsoid. Based on the estimated size s and orientation \mathbf{R}_o of OBE, we obtain

$$\hat{\lambda} i = \left(\frac{s_i}{2\sqrt{\chi_{(p)}^2}} \right)^2 \quad (6)$$

$$\hat{\Sigma} = \mathbf{R}_o \text{diag}(\hat{\lambda}) \mathbf{R}_o^T \quad (7)$$

We set $\chi_{(p)}^2 = \chi_{(0.05)}^2 = 7.815$ to ensure a 95% probability that the ground truth center converges. The derived pseudo-gaussian parameters offer an account of the uncertainty in the segment's center and will be utilized in the compatibility test in Section V-B. Conversely, the statistical Gaussian parameters, which capture the geometric features of the segments, will be

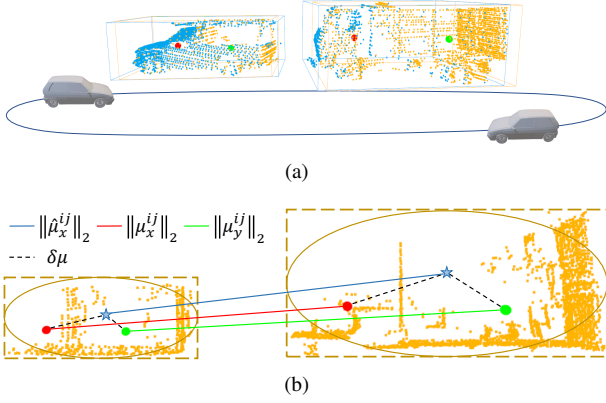


Figure 4. (a) The blue and orange point clouds are from a pair of loop closure frames. The figure shows two clusters and their centers (the red and green spheres represent the centers of the blue and yellow clusters, respectively) with 3D OBBs. (b) The red and green spheres are defined the same as in (a), and the blue pentagrams are the ground truth centers of the two clusters. The deviations of the observed centers from the ground truth are constrained within OBEs tangent to the OBBs. In addition, the translation and rotation invariant measurements (TRIMs) $\|\hat{\mu}_x^{ij}\|_2$ and $\|\mu_x^{ij}\|_2$ and their ground truths $\|\mu_x^{ij}\|_2$ are denoted by the red, green and blue lines, respectively.

used in Section IV-C to build putative correspondences and Section VI-A to estimate the transformation.

C. Soft Association

Starting with a collection of GEMs extracted from the point cloud, we initially select the top-J GEMs from each type of PCL segment. This selection process is based on respective measures of area, volume, and length, as larger segments generally demonstrate superior stability. Following this, we employ a mutual-K-nearest neighbor (MKNN) matching strategy for GEMs that share labels, generating the initial set of putative correspondences represented as \mathcal{I} . This MKNN strategy aids in enhancing the likelihood of including true correspondences. The distance between a pair of GEMs (x, y) utilized in the MKNN is determined by the Wasserstein distance of their statistical covariance matrices,

$$\begin{aligned} \mu'_x &= \mathbf{R}^* \mu_x + \mathbf{t}^* \\ \Sigma'_x &= \mathbf{R}^* \Sigma_x \mathbf{R}^{*T} \end{aligned} \quad (8)$$

$$\begin{aligned} W(f(x | \mathbf{R}^*, \mathbf{t}^*), y) &= \|\mu'_x - \mu_y\|_2^2 \\ &+ \text{Tr} \left(\Sigma'_x + \Sigma_y - 2 \left((\Sigma'_x)^{\frac{1}{2}} \Sigma_y (\Sigma'_x)^{\frac{1}{2}} \right)^{\frac{1}{2}} \right) \end{aligned} \quad (9)$$

In an ideal scenario, the optimal rigid transformation $(\mathbf{R}^*, \mathbf{t}^*)$ is ascertained via Equation (2). However, because it is infeasible during the data association step, we instead derive its substitute $(R_j^o R_i^{oT}, \mu_y - R_j^o R_i^{oT} \mu_x)$ by aligning the two GEMs.

Our proposed MKNN-based association method not only eliminates the need to devise complex descriptors—which are typically employed for one-to-one matching—but also avoids the quadratic growth associated with all-to-all matching. The effectiveness of the Wasserstein distance is validated through comparisons with other metrics in Section VII-B.

V. GRAPH-THEORETIC OUTLIER PRUNING

In this section, we introduce an outlier pruning method based on a pyramid compatibility graph. This approach leverages the compatibility graph (Section V-A), which captures the inter-compatibility among putative correspondences. We assume that inliers will form the maximum clique within this graph. Our framework, operating on a distrust-and-verify scheme, utilizes a multi-threshold compatibility test (Section V-B) to construct a pyramid compatibility graph. Subsequently, a graduated maximum clique solver is introduced (Section V-C) to identify the maximum cliques (MACs) at each level and construct multiple inlier sets. These sets are then employed to generate an array of transformation candidates (Section VI-A).

A. Compatibility Graph Construction

Given a set of GEM correspondences $\mathcal{I} = \{(x_k, y_k)\}$, the centers (μ_x^k, μ_y^k) of each GEM correspondence follows the following model,

$$\begin{aligned} \mu_y^k &= \mathbf{R}^* \mu_x^k + \mathbf{t}^* + \mathbf{o}_k + \epsilon_k \\ \mu_x^k &\sim \mathcal{N}(\hat{\mu}_x^k, \hat{\Sigma}_x^k), \mu_y^k \sim \mathcal{N}(\hat{\mu}_y^k, \hat{\Sigma}_y^k) \\ \epsilon_k &\sim \mathcal{N}(0, \mathbf{R}^* \hat{\Sigma}_x^k \mathbf{R}^{*T} + \hat{\Sigma}_y^k) \end{aligned} \quad (10)$$

where μ , $\hat{\mu}$ and $\hat{\Sigma}$ represent the center, true center and pseudo covariance matrix of the GEM, respectively. For inlier correspondences, \mathbf{o}_k is a zero vector, while for outlier correspondences, it is an arbitrary vector. ϵ_k captures the uncertainty of the GEM center resulting from viewpoint changes and occlusion.

For any pair of correspondences (x_i, y_i) and (x_j, y_j) , we can construct a pairwise invariant using two TRIMs for the compatibility test. TRIMs are defined as $\|\mu_x^i - \mu_x^j\|_2$ and $\|\mu_y^i - \mu_y^j\|_2$, exploiting the length-preserving property of rigid transformation, as shown in Figure 4. The two correspondences pass the compatibility test if their pairwise invariant satisfies the condition:

$$\left| \|\mu_x^i - \mu_x^j\|_2 - \|\mu_y^i - \mu_y^j\|_2 \right| < \delta_{ij} \quad (11)$$

where δ_{ij} is a threshold used to reject potential outliers in this correspondence pair. It is determined based on the pseudo covariance of the four involved GEMs and will be analyzed in detail in Section V-B.

Finally, we construct a compatibility graph by representing each correspondence as a vertex and connecting an edge between two vertices if they pass the compatibility test.

B. Multi-Threshold Compatibility Test

In this section, we delve into the methodology for selecting the appropriate δ_{ij} , an essential parameter that helps ascertain whether a pair of correspondences meet the criteria of the compatibility test. As previously detailed in Section IV-B, we have utilized pseudo Gaussian distribution parameters to

Algorithm 1: Compatibility Graph Construction

Params: Pre-defined p-values $p_1 \geq p_2 \geq \dots \geq p_M$
Input : Initial putative GEM correspondences
 $\mathcal{I} = \{(x_k, y_k) | k = 1 : N\}$
Output: Pyramid graph $\{\mathcal{G}_m | m = 1 : M\}$

```

1 Function ConstructGraphs ( $\mathcal{I}$ )
2   % parallel running
3   for (i, j) in  $\binom{N}{2}$  do
4      $d_{ij} = \left| \|\mu_x^i - \mu_x^j\|_2 - \|\mu_y^i - \mu_y^j\|_2 \right|$ ;
5      $\lambda_{x,1}^{ij} = \text{UpperEigenvalue}(\hat{\Sigma}_x^i, \hat{\Sigma}_x^j)$ ;
6      $\lambda_{y,1}^{ij} = \text{UpperEigenvalue}(\hat{\Sigma}_y^i, \hat{\Sigma}_y^j)$ ;
7     for m = 1 : M do
8        $\delta_{ij} = \sqrt{\chi_{(p_m)}^2 \lambda_{x,1}^{ij}} + \sqrt{\chi_{(p_m)}^2 \lambda_{y,1}^{ij}}$ ;
9       if  $d_{ij} \leq \delta_{ij}$  then
10        for k = m : M do
11           $\mathcal{G}_k.\text{addEdge}(i, j)$ ;
12        end
13        break;
14      end
15    end
16  end
17 End Function
18 Function UpperEigenvalue ( $\Sigma_1, \Sigma_2$ )
19    $\Sigma = \Sigma_1 + \Sigma_2$ ;
20   %Perron Frobenius theorem
21    $\text{ub}_1 = \max \left( \sum_{i=1}^3 |\Sigma_{i,j}| \right) \quad \forall j \in \{1, 2, 3\}$ ;
22   %Wolkowicz's method
23    $m \leftarrow \frac{\text{trace}(\Sigma)}{3}$ ;  $s^2 \leftarrow \frac{\text{trace}(\Sigma^2)}{3} - m^2$ ;
24    $\text{ub}_2 = m + \sqrt{2s^2}$ ;
25   %Weyl's inequality
26    $\text{ub}_3 = \lambda_1(\Sigma_1) + \lambda_1(\Sigma_2)$ ;
27   return (min(ub1, ub2, ub3))
28 End Function

```

effectively model the uncertainty inherent in the center μ . This leads us to the following relationships:

$$\begin{aligned}
\mu_x^i &\sim \mathcal{N}(\hat{\mu}_x^i, \hat{\Sigma}_x^i), \mu_x^j \sim \mathcal{N}(\hat{\mu}_x^j, \hat{\Sigma}_x^j) \\
\mu_y^i &\sim \mathcal{N}(\hat{\mu}_y^i, \hat{\Sigma}_y^i), \mu_y^j \sim \mathcal{N}(\hat{\mu}_y^j, \hat{\Sigma}_y^j) \\
\mu_x^i - \mu_x^j &\sim \mathcal{N}(\hat{\mu}_x^i - \hat{\mu}_x^j, \hat{\Sigma}_x^i + \hat{\Sigma}_x^j) = \mathcal{N}(\hat{\mu}_x^{ij}, \hat{\Sigma}_x^{ij}) \\
\mu_y^i - \mu_y^j &\sim \mathcal{N}(\hat{\mu}_y^i - \hat{\mu}_y^j, \hat{\Sigma}_y^i + \hat{\Sigma}_y^j) = \mathcal{N}(\hat{\mu}_y^{ij}, \hat{\Sigma}_y^{ij})
\end{aligned} \tag{12}$$

Let $\mu_x^{ij} = \mu_x^i - \mu_x^j = \hat{\mu}_x^{ij} + \epsilon_x^{ij}$, where $\epsilon_x^{ij} \sim \mathcal{N}(0, \hat{\Sigma}_x^{ij})$, and $\mu_y^{ij} = \mu_y^i - \mu_y^j = \hat{\mu}_y^{ij} + \epsilon_y^{ij}$, where $\epsilon_y^{ij} \in \mathcal{N}(0, \hat{\Sigma}_y^{ij})$. We consider the two correspondences be both inliers, thus $\hat{\mu}_x^{ij} = \mathbf{R}^* \hat{\mu}_x^{ij}$. According to the triangle inequality, we have

$$\|\mu_x^{ij}\|_2 \leq \|\hat{\mu}_x^{ij}\|_2 + \|\epsilon_x^{ij}\|_2 \tag{13}$$

in which ϵ_x^{ij} characterizes the joint uncertainty between the GEMs μ_x^i and μ_x^j . This joint uncertainty can also be similarly confined within its corresponding uncertainty ellipsoid.

To simplify matters and maintain generality, we adopt the probability p as a means to model this uncertainty, as detailed below:

$$(\epsilon_x^{ij})^T (\hat{\Sigma}_x^{ij})^{-1} \epsilon_x^{ij} \leq \chi_{(p)}^2 \tag{14}$$

where $\hat{\Sigma}_x^{ij}$ is a symmetric and positive-definite matrix that can be expressed in a diagonalized form, as illustrated below:

$$\hat{\Sigma}_x^{ij} = U \begin{bmatrix} \lambda_{x,1}^{ij} & 0 & 0 \\ 0 & \lambda_{x,2}^{ij} & 0 \\ 0 & 0 & \lambda_{x,3}^{ij} \end{bmatrix} U^T \tag{15}$$

where U is an orthogonal matrix and $\lambda_{x,1}^{ij} \geq \lambda_{x,2}^{ij} \geq \lambda_{x,3}^{ij}$. Furthermore, we can get a lower bound on $(\epsilon_x^{ij})^T (\hat{\Sigma}_x^{ij})^{-1} \epsilon_x^{ij}$,

$$\begin{aligned}
&(\epsilon_x^{ij})^T (\hat{\Sigma}_x^{ij})^{-1} \epsilon_x^{ij} \\
&= (U^T \epsilon_x^{ij})^T \begin{bmatrix} \lambda_{x,1}^{ij} & 0 & 0 \\ 0 & \lambda_{x,2}^{ij} & 0 \\ 0 & 0 & \lambda_{x,3}^{ij} \end{bmatrix}^{-1} (U^T \epsilon_x^{ij}) \\
&= \sum_k \frac{1}{\lambda_{x,k}^{ij}} (U^T \epsilon_x^{ij})_k^2 \geq \frac{1}{\lambda_{x,1}^{ij}} \sum_k (U^T \epsilon_x^{ij})_k^2 \\
&= \frac{1}{\lambda_{x,1}^{ij}} (\epsilon_x^{ij})^T \epsilon_x^{ij} = \frac{1}{\lambda_{x,1}^{ij}} \|\epsilon_x^{ij}\|_2^2
\end{aligned} \tag{16}$$

where $\lambda_{x,1}^{ij}$ is the largest eigenvalue of $\hat{\Sigma}_x^{ij}$. By consolidating equations (13), (14) and (16), we can derive an upper bound for $\|\mu_x^{ij}\|_2$, as follows:

$$\begin{aligned}
\|\mu_x^{ij}\|_2 &\leq \|\hat{\mu}_x^{ij}\|_2 + \|\epsilon_x^{ij}\|_2 \\
&\leq \|\hat{\mu}_x^{ij}\|_2 + \sqrt{\chi_{(p)}^2 \lambda_{x,1}^{ij}}
\end{aligned} \tag{17}$$

Following a similar derivation, we can establish the upper bound of $\|\mu_y^{ij}\|_2$ as follows,

$$\begin{aligned}
\|\mu_y^{ij}\|_2 &\leq \|\hat{\mu}_y^{ij}\|_2 + \|\epsilon_y^{ij}\|_2 \\
&\leq \|\mathbf{R}^* \hat{\mu}_y^{ij}\|_2 + \sqrt{\chi_{(p)}^2 \lambda_{y,1}^{ij}} \\
&= \|\hat{\mu}_y^{ij}\|_2 + \sqrt{\chi_{(p)}^2 \lambda_{y,1}^{ij}}
\end{aligned} \tag{18}$$

Finally, by integrating equations (17) and (18), we can determine δ_{ij} by assigning a confidence probability p (e.g., 90%) to accept the observation. It is noteworthy that a larger value of p implies a reduction in uncertainty.

$$\left| \|\mu_x^{ij}\|_2 - \|\mu_y^{ij}\|_2 \right| \leq \sqrt{\chi_{(p)}^2 \lambda_{x,1}^{ij}} + \sqrt{\chi_{(p)}^2 \lambda_{y,1}^{ij}} = \delta_{ij} \tag{19}$$

The comprehensive process of constructing the pyramid graph using a multi-threshold compatibility test is encapsulated in Algorithm 2. For N correspondences, it is necessary to compute the TRIMs and their upper bounds for $N(N-1)/2$ pairs, as indicated in lines 4-6 of Algorithm 2. To reduce the computational burden associated with eigenvalue calculations, we employ the Perron-Frobenius theorem [44, 45], Wolkowicz's method [46], and Weyl's inequality [47]. These techniques aid in computing the upper bound of the largest eigenvalue λ_1 , as presented in line 18, thereby accelerating the computation process.

C. Graduated MAC Solver

Given M p -values $p_1 \geq p_2 \geq \dots \geq p_M$, we correspondingly have χ^2 -values $\chi^2_{(p_1)} \leq \chi^2_{(p_2)} \leq \dots \leq \chi^2_{(p_M)}$. From these, we derive M compatibility graphs \mathcal{G} along with their associated maximum cliques \mathcal{G}^{MC} . Theoretically, as the value of $\chi^2_{(p)}$ increases, δ_{ij} follows the change, which results in more pairwise correspondences passing the compatibility test, thereby leading to denser compatibility graphs \mathcal{G} . We arrange all the consistency graphs \mathcal{G} in the order of their sparsity, placing the sparsest at the top and the densest at the bottom. Our objective is to compute these M maximum cliques \mathcal{G}^{MC} , where their vertices \mathcal{I}_m^* are potential inlier sets of the initial correspondences \mathcal{I} . At each level of the pyramid graph, our goal is to solve the following optimization problem:

$$\begin{aligned} & \underset{\mathcal{I}_m^* \subseteq \{1, \dots, N\}}{\text{maximize}} \quad |\mathcal{I}_m^*| \\ & \text{s.t.} \quad \left| \|\mu_x^i - \mu_x^j\|_2 - \|\mu_y^i - \mu_y^j\|_2 \right| < \delta_{ij}^m, \forall i, j \in \mathcal{I}_m^* \end{aligned} \quad (20)$$

Proposition 1 (Lower Bound of Clique Cardinality). *Given $\chi^2_{(p_{m+1})} > \chi^2_{(p_m)}$, it follows that $|\mathcal{G}_{m+1}^{\text{MC}}| \geq |\mathcal{G}_m^{\text{MC}}|$.*

Proof. Proceeding by contradiction, let us assume the contrary: $\chi^2_{(p_{m+1})} > \chi^2_{(p_m)}$, but $|\mathcal{G}_{m+1}^{\text{MC}}| < |\mathcal{G}_m^{\text{MC}}|$. Let us denote the consistency thresholds corresponding to $\chi^2_{(p_m)}$ and $\chi^2_{(p_{m+1})}$ as δ_{ij}^m and δ_{ij}^{m+1} respectively. Given that $\chi^2_{(p_{m+1})} > \chi^2_{(p_m)}$, we can infer that $\delta_{ij}^{m+1} > \delta_{ij}^m$ for all i, j .

Consider the maximum cliques at levels m and $m+1$:

$$\begin{aligned} & |\mathcal{G}_m^{\text{MC}}| = |\mathcal{I}_m^*| \\ & \text{s.t.} \quad \left| \|\mu_x^i - \mu_x^j\|_2 - \|\mu_y^i - \mu_y^j\|_2 \right| < \delta_{ij}^m, \forall i, j \in \mathcal{I}_m^* \end{aligned} \quad (21)$$

$$\begin{aligned} & |\mathcal{G}_{m+1}^{\text{MC}}| = |\mathcal{I}_{m+1}^*| \\ & \text{s.t.} \quad \left| \|\mu_x^i - \mu_x^j\|_2 - \|\mu_y^i - \mu_y^j\|_2 \right| < \delta_{ij}^{m+1}, \forall i, j \in \mathcal{I}_{m+1}^* \end{aligned} \quad (22)$$

Given that $\delta_{ij}^{m+1} > \delta_{ij}^m$, any feasible set for \mathcal{I}_m^* must also be a feasible set for \mathcal{I}_{m+1}^* . Hence, the cardinality of $|\mathcal{G}_{m+1}^{\text{MC}}|$ must be greater than or equal to that of $|\mathcal{G}_m^{\text{MC}}|$. This contradicts our earlier assumption that $|\mathcal{G}_{m+1}^{\text{MC}}| < |\mathcal{G}_m^{\text{MC}}|$, and consequently, our proof is concluded. \square

Proposition 1 suggests that we can leverage the maximum clique deduced from a sparse clique to produce a lower bound on the cardinality of MAC for the denser compatibility graph of the subsequent level. This insight works well with an efficient parallel maximum clique finder algorithm, PMC [48], enabling us to devise a graduated PMC algorithm that calculates the maximum clique from the top to the bottom of the pyramid compatibility graph. Specifically, the original PMC algorithm is based on a branch-and-bound method and prunes using the core numbers of the vertices. In the graduated PMC, once we have determined the maximum clique from the sparser graph of the preceding layer, we can exclude all nodes in this layer whose degree is less than the cardinality of the clique. This process substantially reduces the search space, as these nodes cannot be included in the final MAC of the current layer, according to Proposition 1.

VI. ROBUST TRANSFORMATION ESTIMATION

In this section, we illustrate how to derive multiple transformation candidates from the M hypothetical inlier sets \mathcal{I}^* utilizing robust estimation methods (Section VI-A). We then examine the selection of the evaluation function g in Eq. 3 from a robust statistics viewpoint, with the goal of identifying the most appropriate transformation from the set of candidates that can optimally align \mathcal{X} and \mathcal{Y} (Section VI-B).

A. Distribution-to-Distribution Registration

Given a hypothetical inlier set $\mathcal{I}^* = (x_k, y_k)$, we reformulate the Equation (2) as a distribution-to-distribution registration problem using the statistical Gaussian parameters of GEMs. Let $\mu_x^k \in \mathcal{N}(\hat{\mu}_x^k, \Sigma_x^k)$ and $\mu_y^k \in \mathcal{N}(\hat{\mu}_y^k, \Sigma_y^k)$, Equation (2) can be written as,

$$\begin{aligned} \mathbf{R}^*, \mathbf{t}^* &= \underset{\mathbf{R} \in \text{SO}(3), \mathbf{t} \in \mathbb{R}^3}{\text{arg min}} \sum_{(\mu_x^k, \mu_y^k) \in \mathcal{I}^*} \min(r(\mu_y^k, \mu_x^k), \bar{c}^2) \\ r(\mu_y^k, \mu_x^k) &= d_k^T (\Sigma_y^k + \mathbf{R} \Sigma_x^k \mathbf{R}^T)^{-1} d_k \\ d_k &= \mu_y^k - (\mathbf{R} \mu_x^k + \mathbf{t}) \end{aligned} \quad (23)$$

where $d_k \sim \mathcal{N}(\hat{\mu}_y^k - (\mathbf{R} \hat{\mu}_x^k + \mathbf{t}), \Sigma_y^k + \mathbf{R} \Sigma_x^k \mathbf{R}^T)$. $\rho(\cdot)$ is now defined as the Truncated Least Squares (TLS) cost, with \bar{c} representing the inlier cost threshold which is initialized by $\chi^2_{(0.01)}$. The minimization of the residual function $r(\cdot)$ is equivalent to maximizing the log-likelihood of the new Gaussian model d_k .

To solve Equation (23), we use graduated non-convexity [27] implemented in GTSAM [49] where the non-minimal global solver is replaced by Levenberg-Marquardt optimization for the reason that there is no closed-form solution for distribution-to-distribution registration problem. In addition, for plane segments, the covariance matrix is regularized by replacing its eigenvalue with $(1, 1, 10^{-3})$ to work as a plane-to-plane registration.

B. Transformation Verification

Given M hypothetical transformations $(\mathbf{R}_m^*, \mathbf{t}_m^*)$, our objective is to construct the evaluation function $g(\cdot)$ to identify the most suitable transformation by resolving Equation (3). Whereas existing approaches endeavor to certify the global optimality of minimizing the objective function, we take a step back to re-think how to design an objective function that accurately reflects the alignment quality of the point clouds. We argue the objective in Equation (23) may be inadequate for two reasons. First, although GEMs recover geometries of \mathcal{X} and \mathcal{Y} maximally, information loss persists since \mathcal{I}^* contains only a subset of all potential correspondences. Second, \mathcal{I}^* unavoidably contains adversarial outliers that the TLS cannot accommodate.

To address this, we leverage the semantic voxel map V from Section IV to verify candidates, as it retains most raw geometric information. Assuming every $(\mathbf{R}_m^*, \mathbf{t}_m^*)$ is optimal, correspondences producing large residuals are considered outliers. Thus, we formulate $g(\cdot)$ based on the Chamfer distance with a new robust kernel $\hat{\rho}(\cdot)$:

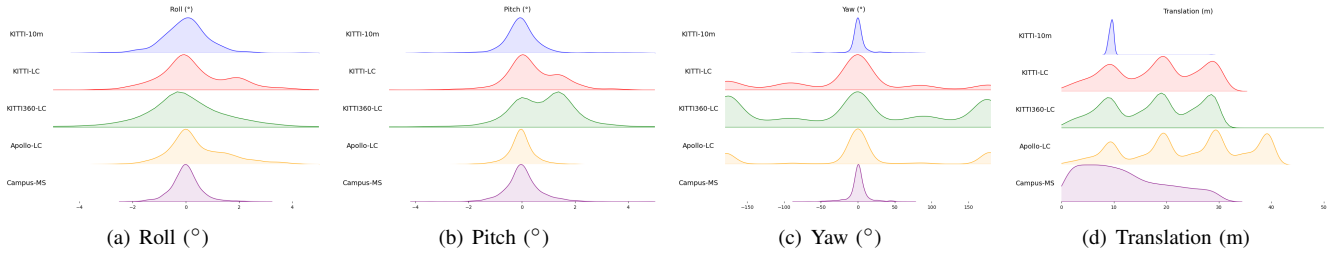


Figure 5. The distributions of ground truth rotations and translations in different datasets. This figure shows broader distributions that can effectively validate global registration performances.

Table I
DATASETS FOR PERFORMANCE EVALUATION

	KITTI-10m	KITTI-loop	KITTI-360	Apollo-SouthBay	Self-collected
Num. of Pairs	556	3325	18469	55118	4707
Testing Strategy	Loop Closure	Loop Closure	Loop Closure	Loop Closure	Multi Sessions
Sensor Type	Velodyne	Velodyne	Velodyne	Velodyne	Livox

$$\begin{aligned}
 g(\mathbf{R}_m^*, \mathbf{t}_m^* | \mathcal{X}, \mathcal{Y}) &= \frac{1}{|\mathcal{X}|} \sum_{v_x \in V_{\mathcal{X}}} \hat{\rho}(r(v'_x, v'_y)) \\
 v'_x &= \mathbf{R}_m^* v_x + \mathbf{t}_m^* \\
 v'_y &= \arg \min_{v_y \in V_{\mathcal{Y}}} \|v'_x - v_y\|_2
 \end{aligned} \quad (24)$$

where $V_{\mathcal{X}}$ and $V_{\mathcal{Y}}$ represent the voxel maps of \mathcal{X} and \mathcal{Y} .

To accelerate the process, we retain only five points per $V_{\mathcal{X}}$ voxel and the center of each $V_{\mathcal{Y}}$ voxel to obtain the compressed raw point clouds. For each sampled v_x , we find the nearest v'_y after applying $(\mathbf{R}_m^*, \mathbf{t}_m^*)$ and compute the residual $r(v'_x, v'_y)$:

$$\begin{cases} |n_y^T(v'_x - v'_y)| & \text{type}(v'_y) = \text{plane} \\ \|\mathbf{I} - d_y^T d_y\| (v'_x - v'_y)\|_2 & \text{type}(v'_y) = \text{line} \\ \|v'_x - v'_y\|_2 & \text{type}(v'_y) = \text{cluster} \end{cases} \quad (25)$$

where n_y and d_y represent the plane normal and the line direction, respectively. We select Dynamic Covariance Scaling (DCS) [50] as $\hat{\rho}(\cdot)$ and contrast it with other kernels including Tukey, Cauchy, Huber [51], and TLS in Section VII-C3.

VII. EXPERIMENTS

This section conducts a comprehensive comparative analysis between our proposed method and existing SOTA techniques, employing various datasets and sensor types. Our method achieves better performance and delivers sub-optimal results with a diminished computational overhead. Additionally, the integration of our novel sub-modules, namely GEM and PAGOR, into any registration approach demonstrates a substantial enhancement in performance. Finally, a review of selected failure cases is also presented to provide practitioners with an in-depth understanding of our methodology.

A. Experimental Setup

1) *Dataset*: As presented in Table I, we conduct experiments on three public and one self-collected multi-session dataset,

namely Campus-MS. The KITTI-10m registration set, widely utilized for the evaluation of LiDAR-based global registration techniques [9, 52, 53], is formed by sampling consecutive frames at 10-meter intervals from sequences 08, 09, and 10 of the KITTI odometry dataset. However, this dataset's concentrated distribution of relative poses between the two point cloud frames may not comprehensively assess the true performance of global registration. Furthermore, the temporal adjacency of these frames introduces a challenge in accurately assessing the impact of environmental variations on point cloud registration.

To address this constraint, we adopt a strategy of sampling registration pairs from revisited locations, a testing approach commonly utilized in re-localization and loop closing scenarios. This approach yields a broader distribution of poses and more pronounced disparities in point cloud data. Furthermore, for any two registration pairs denoted as (P_1, Q_1) and (P_2, Q_2) , we ensure that the translation between P_1 and P_2 , as well as the separation between Q_1 and Q_2 , remains within a threshold of 2 meters. This downsampling procedure is subsequently applied to the registration set to reduce the overall test size. Finally, we leverage the point-to-plane Iterative Closest Point (ICP) algorithm to refine the relative pose estimation of each registration pair within the set, thus generating ground truth pose for the following evaluation sections.

The strategy outlined above is implemented to process three distinct publicly accessible datasets, culminating in the establishment of KITTI-LC [54], KITTI360-LC [55], and Apollo-LC [56] (LC indicates loop closing). These datasets encompass a diverse spectrum of scenarios encountered within the realm of autonomous navigation, encompassing urban downtown locations, highways, overpasses, and suburban environments. We have ensured the public availability of the code used to generate this benchmark dataset, with the intention of benefiting the wider community². The self-collected Campus-MS dataset will be introduced in detail in Section VII-D.

2) *Comparisons*: As mentioned in previous sections, we partition the registration pipeline into two components: the front end and the back end. Concerning the front end, we employ two distinct approaches: the handcrafted descriptor FPFH [3] and the classical deep learning-based descriptor FCGF [4]. As for the back end, our selection encompasses three graph-theoretic methods: TEASER++ [5], Quatro [8], and 3DMAC

²<https://github.com/HKUST-Aerial-Robotics/LiDAR-Registration-Benchmark>

[9], alongside two deep learning-based methods: DGR [52] and PointDSC [53]. Additionally, we incorporate the classic RANSAC method for a comprehensive comparative analysis. We will introduce the settings of these comparisons in the following Section VII-A4. Advanced loop closing methods, like STD [57], Cont2 [58], are also tested as comparisons in this section.

3) *Evaluation metric*: To provide a comprehensive evaluation of performance spanning various levels of difficulty, we partition the test set into three interval subsets based on the translation between the pairs. The partition of test sets is grounded in considerations related to loop closure and robot re-localization scenarios. In the context of deep learning-based place recognition [59, 60], a retrieved pair is considered a true positive if it falls within a radius of 25 meters. It is also worth noting that GPS error typically remains within the range of 30 meters. Thus, the partitioned subsets are denoted as [0, 10] (easy), [10, 20] (medium), and [20, 30] (hard). Notably, the [20, 30] subset presents a higher level of challenge compared to [0, 10] due to the increased distance between the two LiDAR point clouds, leading to a reduced overlap for global registration.

We evaluate the proposed method from three perspectives: *feature matching*, *global registration*, and *computational time consumption*. Feature matching is evaluated through several metrics including the inlier ratio (IR), total number of correspondences, recall, and time consumption. A correspondence (x_i, y_i) is classified as an inlier if it adheres to the following condition:

$$\|\mathbf{R}_{gt}x_i + \mathbf{t}_{gt} - y_i\|_2 < 0.5 \quad (26)$$

where $(\mathbf{R}_{gt}, \mathbf{t}_{gt})$ denote the ground truth rotation and translation, respectively. If the count of inliers within a point cloud pair exceeds 3 (which corresponds to the minimum requirement for 3D registration), that pair is considered successfully recalled. Subsequently, we compute the recall for all pairs in the test set.

For the global registration evaluation, given the estimated transformation $(\mathbf{R}_{est}, \mathbf{t}_{est})$, the registration is classified as successful if

$$\arccos\left(\frac{\text{tr}(\mathbf{R}_{est}^T \mathbf{R}_{gt}) - 1}{2}\right) < 5 \text{ deg} \quad (27)$$

$$\|\mathbf{R}_{est}^T(\mathbf{t}_{gt} - \mathbf{t}_{est})\|_2 < 2\text{m}$$

The rotation and translation thresholds of 5 degrees and 2 meters, respectively, are consistent with the configurations used by other state-of-the-art methods [1, 9, 52]. This metric setting is aligned with the fact that global registration methods typically prioritize robustness, while local registration methods like iterative closest point (ICP) [61] and normal distribution transformation (NDT) [62], emphasize the accuracy of point cloud registration.

4) *Implementation details*: For our proposed method, most of the parameters are in the front-end modules, including ground removal, plane segmentation, cluster segmentation, and line segmentation. For ground removal and clustering, we adopt the default parameters as outlined in their respective

Table II
ALL PARAMETERS OF OUR APPROACH

Parameters			Value
Plane	Extraction	Voxel size s_v	1 m
		λ_2/λ_3 threshold σ_p	30
	Merge	Normal threshold σ_n	0.95
		Distance threshold σ_{p2n}	0.2
Line extraction	Distance threshold σ_{p2l}	0.5 m	
	Inlier ratio threshold σ_{line}	0.5	
Association	Segment number J	50	
	K in MKNN strategy	20	
MAC solver	p-values	[0.99,0.95,0.9,0.8]	
Geometric verification	Robust kernel function	DCS	

original papers [42, 63]. Regarding plane and line segmentation, the relevant six parameters are detailed in Table II. Importantly, a noteworthy aspect is that *we maintain uniformity in parameter application across all experiments, even when the LiDAR type and scenarios vary*. This consistency serves to demonstrate the generalization capability of our proposed method.

For the handcrafted-based FPFH, we carefully balance its efficiency and performance. Specifically, we first remove the ground and downsample the point cloud by voxelization with a 0.5 m resolution. We also finetune the parameters of FPFH, which is 1 m for the normal search radius and 2.5 m for the search radius. As for the deep learning-based FCGF, we directly employ models that have been trained on the KITTI dataset, as provided in their open-source code. Even though the sequence indices of the train set overlap with our test set, such as sequence 00, the point cloud pairs are sampled differently (trained on sequential frames and tested on more challenging loop closure situations). The final correspondences of both FPFH and FCGF are filtered by a mutual nearest neighbor.

Concerning the graph-theoretical methods, we finetune the key parameters to achieve their best performances, which entails setting the noise bound to be 0.4 m for TEASER++ and Quatro, and the compatibility threshold to be 0.9 for 3DMAC. As for RANSAC, the default iteration number is 1,000,000. To expedite the iterative process, we leverage TRIMs with a large threshold to reject incorrect correspondences.

B. Feature Matching Evaluation

In this section, we compare the quality of putative correspondences from the proposed front end using GEM with commonly used descriptor-based methods FPFH [3] and FCGF [4]. The evaluation is conducted using the KITTI-LC dataset, chosen for its close alignment with the domain upon which FCGF has been trained. Additionally, we delve into a comprehensive evaluation of diverse configurations within our proposed methodology, taking into careful consideration factors such as segment types, matching strategies, and the choice of clustering algorithms. This meticulous exploration contributes to a thorough understanding of the efficacy and versatility

Table III
FEATURE MATCHING EVALUATION ON KITTI-LC DATASET

	Method	0-10m				10-20m				20-30m			
		IR (%)	Num	Recall (%)	Time (ms)	IR (%)	Num	Recall (%)	Time (ms)	IR (%)	Num	Recall (%)	Time (ms)
Point-based	FPFH	9.198	642	99.89	170.69	2.575	590	94.52	177.76	0.923	557	64.44	175.16
	FCGF	29.08	2762	96.72	96.21	13.12	2586	87.84	86.52	5.678	2403	71.59	84.12
Segment-based	Plane only	1.109	450	73.08	21.69	0.580	447	42.83	21.87	0.337	441	18.73	22.11
	Line only	2.678	180	56.45	20.65	1.454	185	34.23	21.14	0.741	175	17.38	21.25
	Cluster only	1.677	713	98.03	22.76	0.744	714	81.49	22.77	0.356	712	43.65	23.87
	Ours (Random)	0.618	1737	95.18	24.43	0.342	1753	80.19	24.57	0.203	1738	53.25	25.02
	Ours (IoU3D)	0.418	1379	81.62	24.97	0.270	1381	61.16	24.83	0.175	1361	36.19	25.47
	Ours (EigenVal)	1.159	1379	98.25	24.98	0.562	1377	91.57	25.12	0.302	1356	65.24	25.30
	Ours (FPFH+T)	1.330	1196	98.14	45.38	0.617	1203	89.23	42.58	0.323	1189	60.24	43.34
	Ours (All-to-all)	0.692	3598	99.02	24.41	0.360	3626	96.35	24.50	0.199	3581	85.08	25.77
	Ours (Wass+D)	1.376	1292	96.94	25.12	0.687	1291	92.61	25.10	0.376	1273	71.75	25.27
	Ours (Wass+T)	1.526	1336	<u>98.69</u>	25.02	0.737	1339	<u>94.53</u>	24.80	0.391	1320	<u>74.52</u>	25.17

Table IV
GLOBAL REGISTRATION EVALUATION ON KITTI-10M DATASET

Front-end	Back-end	KITTI-10m				Average Time (ms)
		08	09	10	Total	
FCGF	DGR	96.74	99.38	97.70	97.66	573.34
FCGF	PointDSC	98.37	99.38	98.85	98.74	333.78
FPFH	RANSAC	97.39	100.0	95.40	97.84	264.31
FPFH	TEASER	98.04	98.76	93.10	97.48	236.35
FPFH	3DMAC	95.44	98.15	90.80	95.50	258.29
FPFH	Pagor	99.67	100.0	100.0	99.82	282.38
GEM	RANSAC	83.39	86.42	70.11	82.19	64.68
GEM	TEASER	<u>99.35</u>	99.38	94.25	98.56	45.55
GEM	3DMAC	99.02	100.0	93.10	98.38	55.05
GEM	Pagor	99.34	100.0	<u>98.85</u>	<u>99.46</u>	61.88

of our approach. Specifically, we list the configurations as follows:

- Instead of distinguishing the segment into plane, cluster, and line, we explore the utilization of each category individually.
- We attempt to replace the covariance matrix’s Wasserstein distance with other descriptor-based matchings, such as the IoU of two segments’ bounding boxes (IoU3D), the eigenvalue-based descriptor proposed in [64] (EigenVal), selecting randomly (Random), and enumerating all possible correspondences (All-to-all). Furthermore, a potential limitation is that our descriptor ignores the information of the local structure of the segment. Hence, we follow FPFH to encode this information (FPFH+T) by considering every neighbor (within 20 m) segment’s center and its normal as a point with a normal in the FPFH algorithm (except the normal of the line is replaced by the direction).
- We compare different clustering methods using DCVC [63] (Wass+D) and TRAVEL [42] (Wass+T) to show their influence on our framework.

All the results and findings are shown in Table III. Generally, segment-based matching tends to produce more outliers compared to the point-based method. This disparity arises from the comparatively less robust descriptor employed in segment-based matching, which relies solely on a covariance matrix, as well as the inherent ambiguity in center estimation. Admittedly, a high inlier ratio helps the subsequent estimator reach the global optimal, but with the assistance of MAC, a high outlier ratio can usually be tolerated. The primary concern for MAC is the number of input correspondences as the

computational complexity of MAC exhibits quadratic growth concerning this quantity. For this reason, we still choose the MKNN strategy instead of the all-to-all strategy, despite the latter exhibiting higher recall rates.

Despite the inlier ratio, the recall metric serves as an indicator of the potential success in registering pairs. Notably, as the spatial distance increases, the segment-based method exhibits superior recall compared to the point-based approach. This phenomenon stems from the fact that the efficacy of descriptors like FPFH and FCGF diminishes in response to changes in point density caused by varying distances. Conversely, the utilization of segments as direct entities confers greater robustness in such scenarios. Conversely, the utilization of a fixed threshold (0.5 m) to determine inlier correspondences can be expanded owing to the resilience of our robust registration back-end. Consequently, our proposed segment-based GEM outperforms FPFH and FCGF in subsequent registration experiments, underscoring its superiority.

Table III also presents the ablation study of our method. The comparison of using one of the PCL alone explains why we use plane-aided segmentation and divide segments into different geometric types. Plane segmentation prevents the clustering method from producing large clusters and decreases the randomness of clustering results in different LiDAR point clouds. Moreover, the utilization of such low-level semantics is a lightweight way to scale down the correspondences, thus speeding up the entire registration process. Random selection provides a baseline for different descriptor-based methods. Experimentally, Wasserstein distance-based matching is the best choice. Although it’s not very discriminative, thanks to our MKNN strategy, more possible correspondences are considered, increasing the probability of successful registration. Lastly, the deployment of the TRAVEL clustering module slightly surpasses the performance of the DCVC method. However, it is worth noting that DCVC boasts fewer parameters, thereby affording practitioners the flexibility to choose either option based on their preferences.

C. Registration Evaluation

1) *KITTI-10m Dataset*: Although KITTI-10m is not sufficient to validate the performance of registration as discussed previously, we still present the results in Table IV to maintain the same benchmark as the previous work. Another justification for this is that we found the ground truth provided

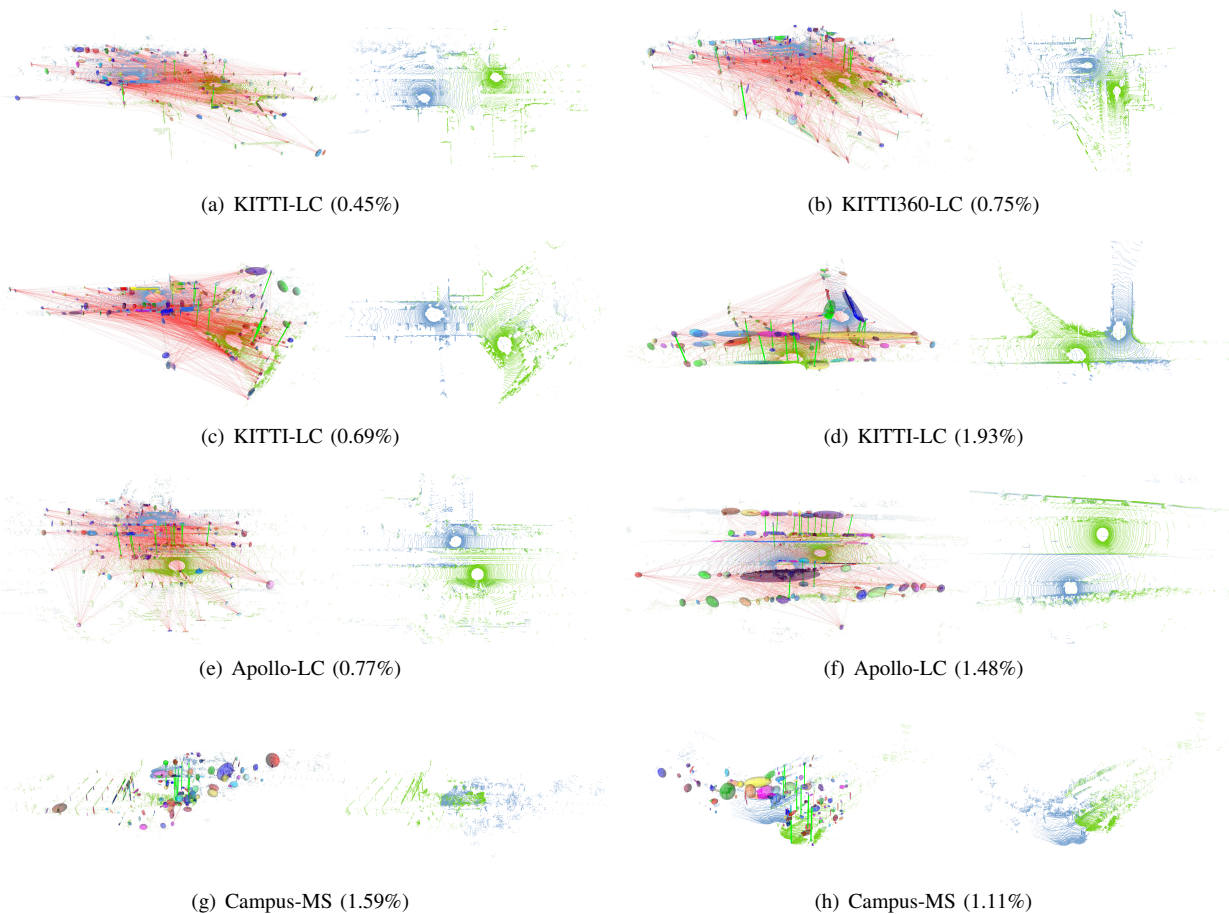


Figure 6. Challenging cases for global registration where G3Reg could achieve successful alignment even when point clouds exhibited low inlier ratios (shown in brackets). (a)-(f) were tested with Velodyne data and (g) and (h) demonstrate registration results using Livox.

ratio situations, such as when using a high-quality descriptor like FPFH and the translation is within 10m. However, as the translation increases and the quality of FPFH decreases, or when using GEM, which has a high outlier ratio, RANSAC does not perform as well as it could not handle too many correspondence outliers in challenging scenarios.

As for graph-theoretical methods, our proposed PAGOR outperforms TEASER++ and Quatro due to our distrust-and-verify framework, with a time increase of only 30 milliseconds. A detailed experiment on time consumption is conducted in Section VII-C3 to help practitioners to balance a trade-off between performance and efficiency.

The conceptual philosophy of 3DMAC aligns closely with ours, both employing a framework of hypothesis generation and evaluation across multiple candidates. Admittedly, the clique consisting of inliers must be the maximal clique as depicted in TEASER [5]. However, the evaluation method proposed in 3DMAC may not find the true one because of the inaccurate estimator SVD and the improper objective function (as mentioned in Section VI-B, the objective function may not represent the degree of alignment). In contrast to 3DMAC, our approach focuses on determining an appropriate threshold to ensure that the true maximal clique coincides with the maximum clique, while also devising a more suitable objective function to assess the generated hypotheses.

In addition to specialized registration methods, we also test advanced loop closure systems with metric pose estimation (STD [57], Cont2 [58]) on the same datasets. We find that STD is sensitive to the physical distance of two point clouds, which we attribute to potential shortcomings in the reproducibility of their feature points (despite increasing the number to 1000). Cont2 performs fairly well with point clouds close to each other, and the speed is noticeably faster than all others, owing to its remarkably efficient scan representation. We note that these methods typically balance recall and precision of loop detection, therefore they could be too conservative for registration-only tasks.

As for the front end, compared to FPFH, our proposed GEM achieves faster speed and more excellent performance with large translations where FPFH descriptor is prone to degradation. More visualizations for GEM matching and registration results on different datasets are shown in Figure 6. Besides that, we also want to show some scenarios where GEM doesn't work. As shown in Figure 8, our method suffers in geometrically uninformative environments where GEMs often exhibit particularly large uncertainties and poor reproducibility. A possible solution to overcoming these limitations could be extracting FPFH within the encompassing range of larger GEM, which could potentially increase the inlier rate.

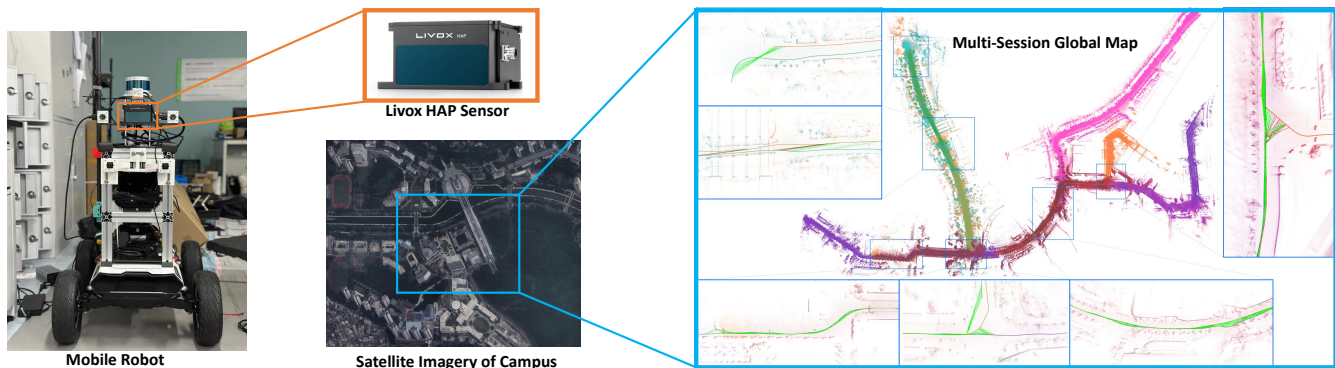


Figure 7. The visualized results of multi-session mapping using our proposed G3Reg. The Campus-MS dataset is collected on a mobile robot platform equipped with a solid-state Livox HAP Sensor. Though the sensor type is different from Velodyne, we still use the same parameter settings for G3Reg. As a result, G3Reg provides stable transformation constraints for the multi-session mapping system (shown in green lines, best viewed in an enlarged format).

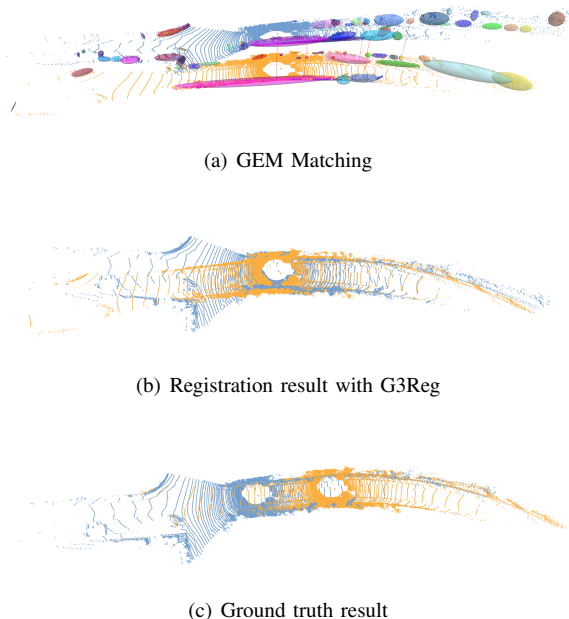


Figure 8. Global registration failure using G3Reg. This is a very challenging case with a vehicle moving on a narrow, geometrically uninformative road. The ground truth translation is 26.18 m.

3) *Ablation Study*: Despite the comprehensive comparisons above, we validate the effectiveness of the main contributions of our method via conducting ablation studies. In addition, we provide a detailed time consumption analysis on correspondences generation (Cor.), pyramid graph construction (Graph), MAC solving (MAC), transformation estimation (Est.) and geometric verification (Verify). This analysis serves as a valuable resource for practitioners, i.e., helping the practitioners to find a balance between performance and efficiency by modifying original G3Reg settings.

Table VIII demonstrates our investigation into two key aspects: the selection of the compatibility threshold δ (Rows 1-9) and the robust kernel function during the verification stage (Rows 10-13). In Row 1-7, we start by considering the smallest probability and progressively incorporate larger probabilities, both individually and in combination. The findings

Table IX
SUCCESS RATE ON CAMPUS-MS DATASET

Front-end	Back-end	Campus-MS					Average Time (ms)
		00	01	02	03	04	
FPFH	TEASER	89.17	94.59	28.57	87.16	89.68	164.88
	Pagor	95.81	99.61	57.14	93.63	96.21	190.91
GEM	TEASER	64.25	55.60	71.43	70.45	65.68	19.54
GEM	Pagor	<u>92.54</u>	94.21	92.86	<u>93.03</u>	<u>94.16</u>	<u>54.78</u>

highlight that any combination of two p-values outperforms the individual counterparts. As we introduce an additional p-value, there is an observable increase in the time required for pyramid graph construction and MAC solving, although this rise is not strictly linear. However, we also find that add a too-large threshold yields only marginal gains in registration performance. These findings suggest that practitioners could strategically select fewer p-value as combinations for a more efficient distrust-and-verify registration.

If we directly use a set of determined values, like 0.2m, 0.4m, 0.6m and 0.8m (Row 8), or replace our proposed pseudo covariance matrix with statistic covariance to compute the compatibility thresholds (Row 9), we find that the performance degrades slightly on challenging [20,30] set and the time consumption slightly increases. This outcome can be attributed to the potential introduction of inaccurate compatibility upper bounds, resulting in an increased presence of unnecessary graph edges that adversely affects efficiency. On the other hand, the performance does not change a lot due to our distrust-and-verify framework. Moving to Row 10-13, we explore various robust kernel functions in Section VI-B. It shows DCS (our default in Row 7), Tukey and TLS exhibit superior experimental performance compared to other alternatives.

D. Real-World Experiments

As introduced in Section VII-A1, we also make a multi-session dataset at a university campus, named Campus-MS, which is collected using a mobile platform equipped with a solid-state LiDAR sensor. This dataset consists of five distinct robot travels (sessions), each collected in different days. To ensure accurate pose ground truth, Real-Time Kinematic (RTK) technology was employed during data collection. For

every frame of one travel, we identify frames in other trips if their overlaps exceed 40%. The quantitative results in Table IX show that our method can still keep its registration efficiency and performance without changing any hyperparameters.

In order to verify the proposed G3Reg in practical applications, we embed it into a map merging task, as shown in Figure 7. Specifically, we first use LiDAR odometry to build subgraphs, then use GPS to find potential loop closures between multiple trajectories. Considering that GPS could not provide stable transformation, we use G3Reg to obtain relative poses and establish loop edges without pose priors. Finally, a global map is achieved by pairwise consistency maximization (PCM) [66] for false loop removal and global pose graph optimization. The precise map merge result demonstrates the effectiveness of G3Reg in practical applications.

VIII. CONCLUSION

In this work, we present G3Reg, an effective and efficient framework for global registration of LiDAR point cloud, addressing the limitations of conventional approaches. G3Reg consists of two primary contributions: GEMs for constructing correspondences and a distrust-and-verify scheme PAGOR. G3Reg significantly improves the robustness and efficiency of global registration. Our extensive evaluations demonstrate superior performance over state-of-the-art methods. In addition, we also analyze the limitations of G3Reg, assisting practitioners in applying our method for various use cases. Our open-source code encourages community exploration and adaptation.

REFERENCES

- [1] P. Yin, S. Yuan, H. Cao, X. Ji, S. Zhang, and L. Xie, "Segregator: Global point cloud registration with semantic and geometric cues," *arXiv preprint arXiv:2301.07425*, 2023. **1, 3, 10**
- [2] H. Yin, X. Xu, S. Lu, X. Chen, R. Xiong, S. Shen, C. Stachniss, and Y. Wang, "A survey on global lidar localization: Challenges, advances and open problems," *arXiv preprint arXiv:2302.07433*, 2023. **1**
- [3] R. B. Rusu, N. Blodow, and M. Beetz, "Fast point feature histograms (fpfh) for 3d registration," in *2009 IEEE international conference on robotics and automation*. IEEE, 2009, pp. 3212–3217. **1, 2, 9, 10**
- [4] C. Choy, J. Park, and V. Koltun, "Fully convolutional geometric features," in *Proceedings of the IEEE/CVF international conference on computer vision*, 2019, pp. 8958–8966. **1, 3, 9, 10**
- [5] H. Yang, J. Shi, and L. Carlone, "Teaser: Fast and certifiable point cloud registration," *IEEE Transactions on Robotics*, vol. 37, no. 2, pp. 314–333, 2020. **1, 3, 9, 13**
- [6] P. C. Lusk, K. Fathian, and J. P. How, "Clipper: A graph-theoretic framework for robust data association," in *2021 IEEE International Conference on Robotics and Automation (ICRA)*. IEEE, 2021, pp. 13 828–13 834. **1, 3**
- [7] J. Shi, H. Yang, and L. Carlone, "Robin: a graph-theoretic approach to reject outliers in robust estimation using invariants," in *2021 IEEE International Conference on Robotics and Automation (ICRA)*. IEEE, 2021, pp. 13 820–13 827. **1, 3**
- [8] H. Lim, S. Yeon, S. Ryu, Y. Lee, Y. Kim, J. Yun, E. Jung, D. Lee, and H. Myung, "A single correspondence is enough: Robust global registration to avoid degeneracy in urban environments," in *2022 International Conference on Robotics and Automation (ICRA)*. IEEE, 2022, pp. 8010–8017. **1, 9**
- [9] X. Zhang, J. Yang, S. Zhang, and Y. Zhang, "3d registration with maximal cliques," in *Proceedings of the IEEE/CVF Conference on Computer Vision and Pattern Recognition*, 2023, pp. 17 745–17 754. **1, 3, 9, 10, 12**
- [10] Z. Qiao, Z. Yu, H. Yin, and S. Shen, "Pyramid semantic graph-based global point cloud registration with low overlap," in *2023 IEEE/RSJ International Conference on Intelligent Robots and Systems (IROS)*, 2023. **1, 2**
- [11] L. Bernreiter, L. Ott, J. Nieto, R. Siegwart, and C. Cadena, "Phaser: A robust and correspondence-free global pointcloud registration," *IEEE Robotics and Automation Letters*, vol. 6, no. 2, pp. 855–862, 2021. **2**
- [12] J. Yang, H. Li, D. Campbell, and Y. Jia, "Go-icp: A globally optimal solution to 3d icp point-set registration," *IEEE transactions on pattern analysis and machine intelligence*, vol. 38, no. 11, pp. 2241–2254, 2015. **2**
- [13] X. Li, J. K. Pontes, and S. Lucey, "Pointnetlk revisited," in *Proceedings of the IEEE/CVF Conference on Computer Vision and Pattern Recognition*, 2021, pp. 12 763–12 772. **2**
- [14] Y. Aoki, H. Goforth, R. A. Srivatsan, and S. Lucey, "Pointnetlk: Robust & efficient point cloud registration using pointnet," in *Proceedings of the IEEE/CVF conference on computer vision and pattern recognition*, 2019, pp. 7163–7172. **2**
- [15] Y. Zhong, "Intrinsic shape signatures: A shape descriptor for 3d object recognition," in *2009 IEEE 12th international conference on computer vision workshops, ICCV Workshops*. IEEE, 2009, pp. 689–696. **2**
- [16] A. Mian, M. Bennamoun, and R. Owens, "On the repeatability and quality of keypoints for local feature-based 3d object retrieval from cluttered scenes," *International Journal of Computer Vision*, vol. 89, pp. 348–361, 2010. **2**
- [17] Y. Cui, Y. Zhang, J. Dong, H. Sun, and F. Zhu, "Link3d: Linear keypoints representation for 3d lidar point cloud," *arXiv preprint arXiv:2206.05927*, 2022. **2**
- [18] X. Bai, Z. Luo, L. Zhou, H. Fu, L. Quan, and C.-L. Tai, "D3feat: Joint learning of dense detection and description of 3d local features," in *Proceedings of the IEEE/CVF conference on computer vision and pattern recognition*, 2020, pp. 6359–6367. **2**
- [19] R. Dubé, D. Dugas, E. Stumm, J. Nieto, R. Siegwart, and C. Cadena, "Segmatch: Segment based place recognition in 3d point clouds," in *2017 IEEE International Conference on Robotics and Automation (ICRA)*. IEEE, 2017, pp. 5266–5272. **2**
- [20] G. Pramatarov, D. De Martini, M. Gadd, and P. Newman, "Boxgraph: Semantic place recognition and pose estimation from 3d lidar," in *2022 IEEE/RSJ International Conference on Intelligent Robots and Systems (IROS)*. IEEE, 2022, pp. 7004–7011. **2**
- [21] H. Deng, T. Birdal, and S. Ilic, "Ppfnet: Global context aware local features for robust 3d point matching," in *Proceedings of the IEEE conference on computer vision and pattern recognition*, 2018, pp. 195–205. **2**
- [22] Z. J. Yew and G. H. Lee, "Rpm-net: Robust point matching using learned features," in *Proceedings of the IEEE/CVF conference on computer vision and pattern recognition*, 2020, pp. 11 824–11 833. **2**
- [23] F. Tombari, S. Salti, and L. Di Stefano, "Unique signatures of histograms for local surface description," in *Computer Vision—ECCV 2010: 11th European Conference on Computer Vision, Heraklion, Crete, Greece, September 5–11, 2010, Proceedings, Part III 11*. Springer, 2010, pp. 356–369. **2**
- [24] S. Ao, Q. Hu, B. Yang, A. Markham, and Y. Guo, "Spinnet: Learning a general surface descriptor for 3d point cloud registration," in *Proceedings of the IEEE/CVF conference on computer vision and pattern recognition*, 2021, pp. 11 753–11 762. **2**
- [25] F. Poesi and D. Boscaini, "Learning general and distinctive 3d local deep descriptors for point cloud registration," *IEEE Transactions on Pattern Analysis and Machine Intelligence*, 2022. **3**
- [26] H. Wang, Y. Liu, Q. Hu, B. Wang, J. Chen, Z. Dong, Y. Guo, W. Wang, and B. Yang, "Roreg: Pairwise point cloud registration with oriented descriptors and local rotations," *IEEE Transactions on Pattern Analysis and Machine Intelligence*, 2023. **3**
- [27] H. Yang, P. Antonante, V. Tzoumas, and L. Carlone, "Graduated non-convexity for robust spatial perception: From non-minimal solvers to global outlier rejection," *IEEE Robotics and Automation Letters*, vol. 5, no. 2, pp. 1127–1134, 2020. **3, 8**
- [28] D. G. Lowe, "Distinctive image features from scale-invariant keypoints," *International journal of computer vision*, vol. 60, pp. 91–110, 2004. **3**
- [29] A. P. Bustos and T.-J. Chin, "Guaranteed outlier removal for point cloud registration with correspondences," *IEEE transactions on pattern analysis and machine intelligence*, vol. 40, no. 12, pp. 2868–2882, 2017. **3**
- [30] O. Enqvist, K. Josephson, and F. Kahl, "Optimal correspondences from pairwise constraints," in *2009 IEEE 12th international conference on computer vision*. IEEE, 2009, pp. 1295–1302. **3**
- [31] J. Yang, X. Zhang, S. Fan, C. Ren, and Y. Zhang, "Mutual voting for ranking 3d correspondences," *IEEE Transactions on Pattern Analysis and Machine Intelligence*, 2023. **3**
- [32] T. Bailey, E. M. Nebot, J. Rosenblatt, and H. F. Durrant-Whyte, "Data association for mobile robot navigation: A graph theoretic approach,"

- in *Proceedings 2000 ICRA. Millennium Conference. IEEE International Conference on Robotics and Automation. Symposia Proceedings (Cat. No. 00CH37065)*, vol. 3. IEEE, 2000, pp. 2512–2517. **3**
- [33] P. C. Lusk, D. Parikh, and J. P. How, “Graffmatch: Global matching of 3d lines and planes for wide baseline lidar registration,” *IEEE Robotics and Automation Letters*, vol. 8, no. 2, pp. 632–639, 2022. **3**
- [34] L. Carlone, “Estimation contracts for outlier-robust geometric perception,” *arXiv preprint arXiv:2208.10521*, 2022. **3**
- [35] D. Chetverikov, D. Svirko, D. Stepanov, and P. Krsek, “The trimmed iterative closest point algorithm,” in *2002 International Conference on Pattern Recognition*, vol. 3. IEEE, 2002, pp. 545–548. **3**
- [36] L. Peng, M. C. Tsakiris, and R. Vidal, “Arcs: Accurate rotation and correspondence search,” in *Proceedings of the IEEE/CVF Conference on Computer Vision and Pattern Recognition*, 2022, pp. 11 153–11 163. **3**
- [37] J. Wu, Y. Zheng, Z. Gao, Y. Jiang, X. Hu, Y. Zhu, J. Jiao, and M. Liu, “Quadratic pose estimation problems: Globally optimal solutions, solvability/observability analysis, and uncertainty description,” *IEEE Transactions on Robotics*, vol. 38, no. 5, pp. 3314–3335, 2022. **3**
- [38] Q.-Y. Zhou, J. Park, and V. Koltun, “Fast global registration,” in *Computer Vision—ECCV 2016: 14th European Conference, Amsterdam, The Netherlands, October 11–14, 2016, Proceedings, Part II 14*. Springer, 2016, pp. 766–782. **3**
- [39] T.-J. Chin, Z. Cai, and F. Neumann, “Robust fitting in computer vision: Easy or hard?” in *Proceedings of the European Conference on Computer Vision (ECCV)*, 2018, pp. 701–716. **3**
- [40] M. J. Black and A. Rangarajan, “On the unification of line processes, outlier rejection, and robust statistics with applications in early vision,” *International journal of computer vision*, vol. 19, no. 1, pp. 57–91, 1996. **3**
- [41] A. Segal, D. Haehnel, and S. Thrun, “Generalized-icp,” in *Robotics: science and systems*, vol. 2, no. 4. Seattle, WA, 2009, p. 435. **3**
- [42] M. Oh, E. Jung, H. Lim, W. Song, S. Hu, E. M. Lee, J. Park, J. Kim, J. Lee, and H. Myung, “Travel: Traversable ground and above-ground object segmentation using graph representation of 3d lidar scans,” *IEEE Robotics and Automation Letters*, vol. 7, no. 3, pp. 7255–7262, 2022. **4, 5, 10, 11**
- [43] H. Freeman and R. Shapira, “Determining the minimum-area encasing rectangle for an arbitrary closed curve,” *Communications of the ACM*, vol. 18, no. 7, pp. 409–413, 1975. **5**
- [44] O. Perron, “Zur theorie der matrices,” *Mathematische Annalen*, vol. 64, no. 2, pp. 248–263, 1907. **7**
- [45] G. Frobenius, F. G. Frobenius, F. G. Frobenius, and G. Mathematician, *Über Matrizen aus nicht negativen Elementen*. Königliche Akademie der Wissenschaften Berlin, 1912. **7**
- [46] H. Wolkowicz and G. P. Styan, “Bounds for eigenvalues using traces,” *Linear algebra and its applications*, vol. 29, pp. 471–506, 1980. **7**
- [47] H. Weyl, “Das asymptotische verteilungsgesetz der eigenwerte linearer partieller differentialgleichungen (mit einer anwendung auf die theorie der hohlraumstrahlung),” *Mathematische Annalen*, vol. 71, no. 4, pp. 441–479, 1912. **7**
- [48] R. A. Rossi, D. F. Gleich, and A. H. Gebremedhin, “Parallel maximum clique algorithms with applications to network analysis,” *SIAM Journal on Scientific Computing*, vol. 37, no. 5, pp. C589–C616, 2015. **8**
- [49] F. Dellaert and G. Contributors, “borglab/gtsam,” May 2022. [Online]. Available: <https://github.com/borglab/gtsam> **8**
- [50] P. Agarwal, G. D. Tipaldi, L. Spinello, C. Stachniss, and W. Burgard, “Robust map optimization using dynamic covariance scaling,” in *2013 IEEE International Conference on Robotics and Automation*. Ieee, 2013, pp. 62–69. **9**
- [51] Z. Zhang, “Parameter estimation techniques: A tutorial with application to conic fitting,” *Image and vision Computing*, vol. 15, no. 1, pp. 59–76, 1997. **9**
- [52] C. Choy, W. Dong, and V. Koltun, “Deep global registration,” in *Proceedings of the IEEE/CVF conference on computer vision and pattern recognition*, 2020, pp. 2514–2523. **9, 10**
- [53] X. Bai, Z. Luo, L. Zhou, H. Chen, L. Li, Z. Hu, H. Fu, and C.-L. Tai, “Pointdsc: Robust point cloud registration using deep spatial consistency,” in *Proceedings of the IEEE/CVF Conference on Computer Vision and Pattern Recognition*, 2021, pp. 15 859–15 869. **9, 10**
- [54] A. Geiger, P. Lenz, and R. Urtasun, “Are we ready for autonomous driving? the kitti vision benchmark suite,” in *2012 IEEE conference on computer vision and pattern recognition*. IEEE, 2012, pp. 3354–3361. **9**
- [55] Y. Liao, J. Xie, and A. Geiger, “Kitti-360: A novel dataset and benchmarks for urban scene understanding in 2d and 3d,” *IEEE Transactions on Pattern Analysis and Machine Intelligence*, vol. 45, no. 3, pp. 3292–3310, 2022. **9**
- [56] W. Lu, G. Wan, Y. Zhou, X. Fu, P. Yuan, and S. Song, “Deepvcv: An end-to-end deep neural network for point cloud registration,” in *Proceedings of the IEEE/CVF international conference on computer vision*, 2019, pp. 12–21. **9**
- [57] C. Yuan, J. Lin, Z. Zou, X. Hong, and F. Zhang, “Std: Stable triangle descriptor for 3d place recognition,” *arXiv preprint arXiv:2209.12435*, 2022. **10, 13**
- [58] B. Jiang and S. Shen, “Contour context: Abstract structural distribution for 3d lidar loop detection and metric pose estimation,” in *2023 IEEE International Conference on Robotics and Automation (ICRA)*, London, United Kingdom, 2023, p. 8386–8392. **10, 13**
- [59] M. A. Uy and G. H. Lee, “Pointnetvlad: Deep point cloud based retrieval for large-scale place recognition,” in *Proceedings of the IEEE conference on computer vision and pattern recognition*, 2018, pp. 4470–4479. **10**
- [60] Z. Liu, S. Zhou, C. Suo, P. Yin, W. Chen, H. Wang, H. Li, and Y.-H. Liu, “Lpd-net: 3d point cloud learning for large-scale place recognition and environment analysis,” in *Proceedings of the IEEE/CVF International Conference on Computer Vision*, 2019, pp. 2831–2840. **10**
- [61] P. J. Besl and N. D. McKay, “Method for registration of 3-d shapes,” in *Sensor fusion IV: control paradigms and data structures*, vol. 1611. Spie, 1992, pp. 586–606. **10**
- [62] M. Magnusson, A. Lilienthal, and T. Duckett, “Scan registration for autonomous mining vehicles using 3d-ndt,” *Journal of Field Robotics*, vol. 24, no. 10, pp. 803–827, 2007. **10**
- [63] P. Zhou, X. Guo, X. Pei, and C. Chen, “T-loam: truncated least squares lidar-only odometry and mapping in real time,” *IEEE Transactions on Geoscience and Remote Sensing*, vol. 60, pp. 1–13, 2021. **10, 11**
- [64] M. Weinmann, B. Jutzi, and C. Mallet, “Semantic 3d scene interpretation: A framework combining optimal neighborhood size selection with relevant features,” *ISPRS Annals of the Photogrammetry, Remote Sensing and Spatial Information Sciences*, vol. 2, pp. 181–188, 2014. **11**
- [65] J. Behley, M. Garbade, A. Milioto, J. Quenzel, S. Behnke, J. Gall, and C. Stachniss, “Towards 3D LiDAR-based semantic scene understanding of 3D point cloud sequences: The SemanticKITTI Dataset,” *The International Journal on Robotics Research*, vol. 40, no. 8-9, pp. 959–967, 2021. **12**
- [66] J. G. Mangelson, D. Dominic, R. M. Eustice, and R. Vasudevan, “Pairwise consistent measurement set maximization for robust multi-robot map merging,” in *2018 IEEE international conference on robotics and automation (ICRA)*. IEEE, 2018, pp. 2916–2923. **15**